Scripta Materialia 259 (2025) 116525

Contents lists available at ScienceDirect

Scripta Materialia

journal homepage: www.journals.elsevier.com/scripta-materialia

# Effect of WC/WC grain boundary misorientation angle on the local hardness in WC–Co cemented carbides

Hansheng Chen [a,b,1], Haoruo Zhou [a,b,1], Xiangyuan Cui [a,b], Christoph Czettl [c], Thomas Weirather [c], Julia Pachlhofer [c], Pauline Mueller [c], Tamara Teppernegg [c], Ralph Useldinger [d], Sophie Primig [e], Simon P. Ringer [a,b,*]

[a] School of Aerospace, Mechanical and Mechatronic Engineering, The University of Sydney, Sydney, NSW 2006, Australia
[b] Australian Centre for Microscopy and Microanalysis, The University of Sydney, Sydney, NSW 2006, Australia
[c] CERATIZIT Austria GmbH, Metallwerk-Plansee-Straße 71, 6600 Reutte, Austria
[d] CERATIZIT Luxembourg S.à.r.l., 101 Route de Holzem, 8232 Mamer, Luxemburg
[e] School of Materials Science & Engineering, UNSW Sydney, NSW 2052, Australia

ARTICLE INFO

*Keywords:*
WC–Co cemented carbide
90° $WC_{\{0001\}}/WC_{\{1010\}}$ grain boundary
Hardness
Segregation

ABSTRACT

Grain boundaries (GBs) generally exhibit complex structural and compositional features that significantly affect material hardness. Here, we establish a methodology to correlate the local hardness contributions of the GBs with their frequency distribution and their structural and compositional characteristics, using a submicron WC–Co cemented carbide as a model. An exceptional local hardness of (14.68 ± 0.12) GPa is observed from a 90° $WC_{\{0001\}}/WC_{\{10\bar{1}0\}}$ GB, unlike the low contributions from other WC/WC GBs. This is linked to pronounced Cr and Co segregation at this GB, due to Cr affinity at the $WC_{\{0001\}}$/Co and $WC_{\{10\bar{1}0\}}$/Co phase boundaries and Co infiltration during liquid-phase sintering. Density functional theory results indicate that a large lattice mismatch, strong W–C covalent bonding, and Cr and Co accumulation increase the elastic strain field, resulting in strong atomic distortion near the interface and contributing to exceptional strengthening. Our findings highlight the critical influence of GB complexities on material hardness.

A grain boundary (GB) serves as the interface between adjacent grains that possess different crystallographic orientations in polycrystalline materials [1,2]. As one of the most prevalent defects, GBs play a pivotal role in determining several properties, such as mechanical strength and hardness [3,4], fracture toughness [5], corrosion resistance [6], electrical conductivity [7], and magnetic coercivity [8]. Notably, research on GBs often emphasizes the average grain size as a pivotal factor. For example, the classical Hall–Petch relationship describes how yield stress in materials is enhanced by decreasing the average grain size, which increases the density of the GBs for obstructing dislocation motion [9,10]. However, GBs, characterised by their six macroscopic degrees of freedom (5 crystallographic and 1 chemistry), often exhibit complexity in their atomic structure and composition [11]. Such intricacies are equally, if not more, influential in determining GB-associated properties than just the average grain size.

WC–Co cemented carbides are a crucial class of hard metals used in various industrial processes, such as metal cutting, drilling, and mining, owing to their high hardness and wear resistance [12]. These materials consist of tungsten carbide (WC) grains embedded in Co binder grains, with WC grain sizes ranging from a few micrometres to several hundred nanometres [12]. The performance of these materials is significantly influenced by their microstructure, particularly the size and distribution of WC grains and the characteristics of the WC/WC grain boundaries. Ru is believed to increase the hardness of WC–Co cemented carbides [13,14]. The incorporation of grain growth inhibitors (GGIs), such as $Cr_3C_2$, is also believed to increase the hardness of WC–Co cemented carbides by increasing the density of the WC/WC GBs [15–17].

Co segregation at WC/WC GBs and its potential strengthening effect has been well reported. Experimental results have shown Co segregation levels between 3.1 and 6.1 at.% at some WC/WC GBs [18], although no clear relationship between the misorientation angle of these WC/WC GBs and the level of Co segregation was found [19]. Several *ab initio*

* Corresponding author.
*E-mail address:* simon.ringer@sydney.edu.au (S.P. Ringer).
[1] Equally contributed to this work.

https://doi.org/10.1016/j.scriptamat.2024.116525
Received 11 September 2024; Received in revised form 26 November 2024; Accepted 18 December 2024
Available online 20 January 2025

calculations have further predicted the strengthening effect from Co segregation at specific GBs, such as the Σ2 WC/WC GB [20,21]. The most significant strengthening effect was reported when Co substitutes for carbon in carbon-terminated boundaries [20].

Studies have also investigated Cr segregation at WC/WC GBs and the resulting strengthening effects. Experimentally, Cr segregation levels of 1.1 and 2.6 at.% have been observed at some WC/WC GBs, and *ab initio* calculations have demonstrated that Cr segregation induces significant strengthening [18,20]. However, the crystallographic nature of these WC/WC GBs, such as misorientation angle, remains unknown. Consequently, there is limited experimental knowledge on the relationship between the crystallographic nature of WC/WC GBs and potential Cr segregation.

Recent advancements in microscopy techniques, such as aberration-corrected (scanning) transmission electron microscopy (S/TEM), energy dispersive X-ray spectroscopy (EDXS), transmission Kikuchi diffraction (TKD), and atom probe tomography (APT), have empowered researchers to probe the structural and compositional characteristics of GBs at the atomic level [22,23]. While these techniques yield detailed insights into the structure and chemistry of specific individual GBs, conventional methods for measuring the material hardness, such as the Vickers hardness test, only assess the entire polycrystalline sample and therefore encompass diverse GB types. Such an approach obscures the direct 1:1 correlation between local hardness imparted by individual GBs and their unique structural and compositional characteristics. Fortunately, nanoindentation offers a great possibility for assessing the local hardness contributed by individual GBs [24].

In this context, we introduce a methodology that integrates nanoindentation, scanning electron microscopy (SEM), electron backscatter diffraction (EBSD), correlative TKD and STEM–EDXS, and APT techniques. This synergistic combination is designed to elucidate a precise 1:1 correlation between local hardness imparted by individual GBs, their frequency distribution, and their unique structural and compositional characteristics, as exemplified in a tungsten carbide–cobalt (WC–Co) cemented carbide.

The submicron WC–10Co–1.5 ruthenium (Ru)–0.6 chromium carbide ($Cr_3C_2$) by weight percentage (wt.%) cemented carbide was supplied by CERATIZIT Austria GmbH and used in this study. The detailed experimental procedure can be found in Supplementary Information. The first-principles calculations were performed based on density functional theory (DFT) using the projector augmented wave method [25] and the generalised gradient approximation [26], as implemented in the Vienna Ab initio Simulation Package (VASP) [27].

Fig. 1 presents a schematic illustration of this experimental methodology which integrates nanoindentation, SEM, EBSD, TKD, STEM–EDXS, and APT. We first conducted nanoindentation measurements across a 20 × 20 array to measure the local hardness within the area of ~50 × 50 μm$^2$, maintaining a consistent load force of 5 mN (Fig. S1). Subsequently, SEM and EBSD analyses were performed to determine if the indent was placed on an intragranular WC grain, at an individual WC/WC GB, or at multiple WC/WC GBs and triple junctions among several WC grains.

We were particularly interested in the indents placed on an individual WC/WC GB between two WC grains (Fig. 1A). The hardness contribution by the individual WC/WC GB ($H_{WC1/WC2\ GB}$) was estimated using the rule of mixture: $H_{WC1/WC2\ GB} = H_{experiment} - H_{WC1}V_{WC1} - H_{WC2}V_{WC2}$. Here, $H_{experiment}$ corresponds to the measured local hardness of the indent placed on the individual WC1/WC2 GB. $H_{WC1}$ and $H_{WC2}$ represent the hardness values of the two adjacent WC grains (Table S1). $V_{WC1}$ and $V_{WC2}$ denote their respective volume fractions (Fig. S2 and Supplementary Text). The values for $H_{WC1}$ and $H_{WC2}$ were obtained either directly using the intragranular hardness values closest to the

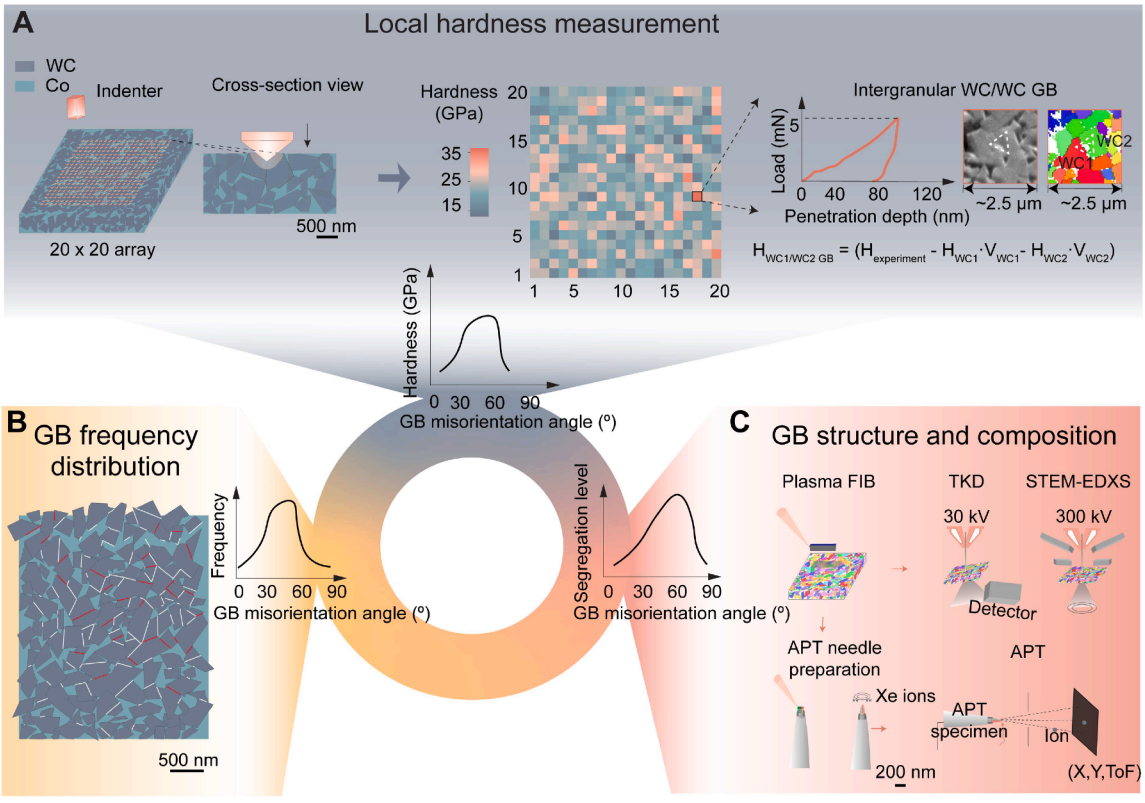


**Fig. 1. Integrated methodology combining nanoindentation with high-end correlative microscopy techniques.** (**A**) Nanoindentation hardness measurements across a 20 × 20 array. Subsequent use of SEM and EBSD techniques to estimate the hardness contribution by a single WC/WC GB relative to its misorientation angle. (**B**) EBSD analysis to chart the occurrence frequency of the WC/WC GBs in correlation to their misorientation angles. (**C**) Correlative TKD and STEM–EDXS, and APT measurements to uncover the level of elemental segregation at individual WC/WC GBs as a function of their misorientation angles.

orientation of the adjacent WC grains when the difference between the two nearest measured intragranular WC grain hardness values is within 3 GPa, or applying a linear fit to the hardness values between the two nearest intragranular hardness data points when the difference exceeds 3 GPa (Tables S2–S3, Fig. S3, and Supplementary Text). By integrating the insights from nanoindentation, SEM, and EBSD techniques, we could swiftly pinpoint the local hardness values contributed by the individual WC/WC GBs in relation to their misorientation angles.

Following the verification of the WC/WC GB-related local hardness, we performed additional EBSD analyses within an SEM to chart the occurrence of the WC/WC GBs as a function of their misorientation angles (Fig. 1B). We further conducted correlative TKD and STEM–EDXS, and APT experiments to reveal the difference in the level of elemental segregation at the individual WC/WC GBs as a function of their misorientation angles (Fig. 1C). In detail, a thin lamella, containing plenty of the WC grains and the WC/WC GBs, was 'lifted-out' using a manipulator in a dual-beam plasma focussed ion beam (pFIB) system. This lamella was then placed in a 30 kV SEM to perform the TKD mapping, allowing us to select a few individual WC/WC GBs and measure their misorientation angles. Subsequently, this identical lamella was transferred to a 300 kV (S)TEM for STEM–EDXS mapping (Table S4 and Supplementary Text), aimed at investigating the elemental

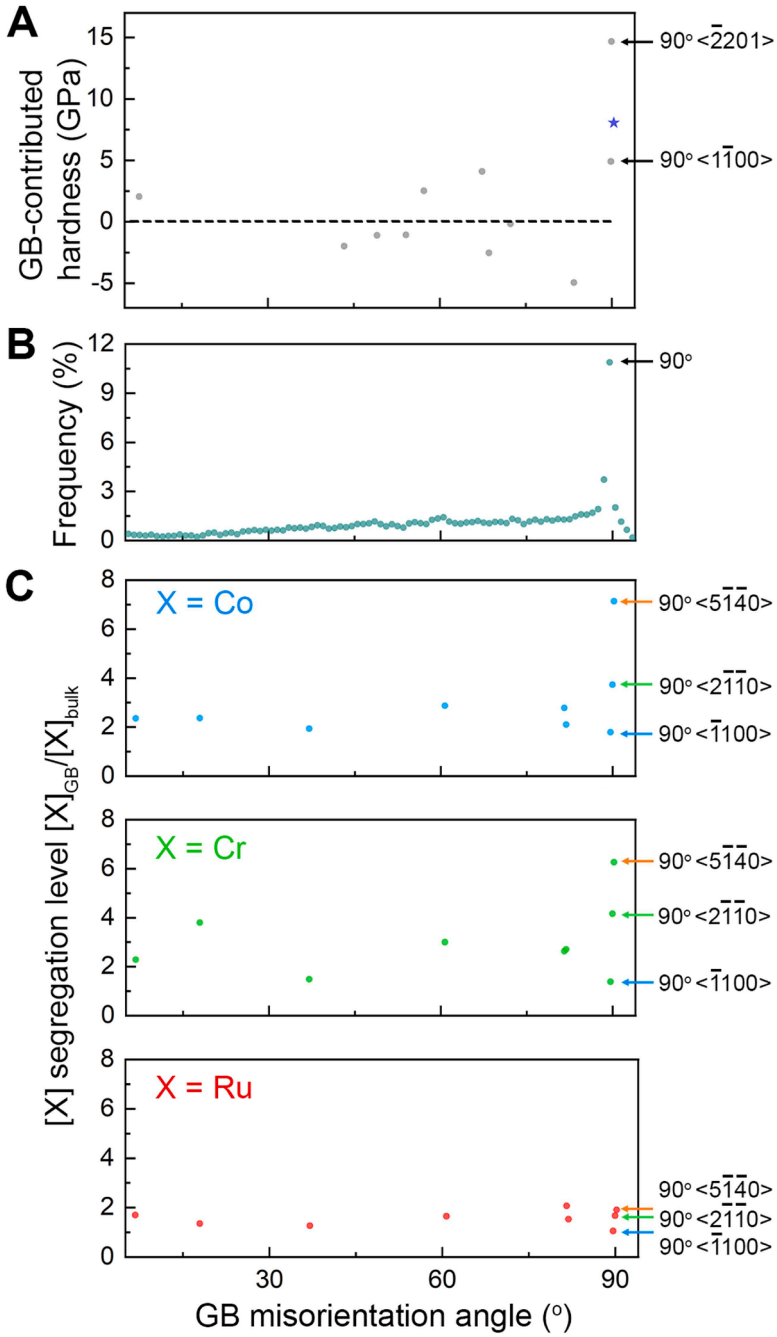


**Fig. 2. Misorientation angle-dependent GB local hardness, distribution, and segregation levels in the submicron WC–10Co–1.5Ru–0.6$Cr_3C_2$ cemented carbide.** (**A**) The local hardness contributed by individual WC/WC GBs, plotted as a function of their misorientation angles. (**B**) Distribution of the WC/WC GBs charted relative to their misorientation angles. The combined frequency of the 90° WC/WC GBs is particularly highlighted. (**C**) Segregation levels of Co, Cr, and Ru at individual WC/WC GBs, examined in relation to their misorientation angles. Segregation level is defined by the concentration ratio (at.%) of these elements, as detected by STEM–EDXS, between the WC/WC GB and the adjacent WC grains. A total of nine WC/WC GBs were analysed.

segregation across the same WC/WC GBs initially identified by TKD. We also prepared a tip containing an individual WC/WC GB for APT analysis, which helped calibrate the concentration levels measured by STEM–EDXS. It is important to note that while STEM–EDXS does not provide a precise compositional analysis, it does facilitate reliable comparative assessments of the concentration ratios between various regions of interest and across different samples. In contrast, APT provides accurate compositional data, though obtaining crystallographic information can sometimes be complex.

Fig. 2 presents the GB misorientation angle-dependent local hardness, frequency distribution, and segregation levels. Fig. 2A and Table S5 illustrate the hardness contributed by individual WC/WC GBs in relation to their misorientation angles. Among 400 datapoints, 11 are showcased here. Figs. S4–S6 present forescatter electron (FSE) and inverse pole figure-Z (IPF-Z) images, as well as corresponding load–displacement curves of the indents placed on the individual WC/WC GBs with misorientation angles ranging from 7° to 90°. Specifically, the average hardness contributed by the WC/WC GBs with misorientation angles ranging from 7 to 90° (except the non-coherent 90°) is calculated to be 0.19 ± 2.97 GPa. This suggests that the strengthening effect of these WC/WC GBs is moderate.

The coherent coincident site lattice (CSL) Σ2 90°<1$\bar{1}$00> WC/WC GB is observed to possess a significantly high hardness value of 4.92 ± 0.14 GPa (Fig. 2A and Fig. S6). This aligns with expectations, as coherent 90°<10$\bar{1}$0> WC/WC GB are known to exhibit enhanced strength compared to other high-angle WC/WC GBs, primarily due to their increased resistance to dislocation propagation [28,29].

Unexpectedly, the 90°<$\bar{2}$201> WC/WC GB is observed to contribute to an exceptionally high local hardness contribution of 14.68 ± 0.12 GPa (Fig. 2A and Fig. S5), markedly surpassing that of other GBs. Similarly, another 90°<1$\bar{5}$40> WC/WC GB in another submicron WC–Co cemented carbide also exhibits an extremely high local hardness contribution of 8.06 ± 1.09 GPa, as indicated by the blue star in Fig. 2A and Fig. S6. It is also noticed that the indents placed on multiple WC/WC GBs and triple junctions including these 90° GBs also exhibited relatively high hardness values (Fig. S7 and Table S6).

Fig. 2B presents the frequency distribution of the WC/WC GBs as a function of their misorientation angles. The frequency exhibits a gradual increase with the WC/WC GB misorientation angle until it reaches 88°. Among the WC/WC GBs examined, 17.78 % display a misorientation angle of 90°, considering a tolerance of ±2° (Fig. S8). This percentage comprises both the coherent and the non-coherent types: 8.44 % are coherent 90°<10$\bar{1}$0> WC/WC GBs, while the remaining 9.34 % are non-coherent 90° WC/WC GBs (Table S7).

Fig. 2C illustrates the segregation levels of Co, Cr, and Ru at the WC/WC GBs in relation to their misorientation angles. Nine individual WC/WC GBs with misorientation angles ranging from 7 to 90° were investigated using the correlative TKD and STEM–EDXS techniques (Fig. S9 and Fig. S10). With the GB misorientation angle increasing from 7° to 82°, the levels of Cr, Co, and Ru segregation are found to remain relatively constant, with the concentration ratios of 1.5–3.8, 1.9–2.9, and 1.3–2.1, respectively (Fig. 2C and Table S8). The coherent 90°<10$\bar{1}$0> WC/WC GB exhibits virtually no segregation of Co (1.8), Cr (1.4), and Ru (1.1), aligning with expectations. By contrast, pronounced segregation of Cr and Co is observed at two non-coherent 90° WC/WC GBs. The exact compositional data obtained using APT also presents strong segregation of Cr (9.7 at.%) and Co (13.1 at.%) at a randomly selected WC/WC GB (Fig. S11, Fig. S12, and Table S8).

To investigate the orientation relationship between neighbouring WC grains across these 90° WC/WC GBs, high-resolution TEM (HRTEM) was performed. It is noteworthy that the $WC_{\{0001\}}$ and $WC_{\{10\bar{1}0\}}$ planes are considered to play significant roles in Co and Cr segregation at these 90° WC/WC GBs. Fig. 3A presents the HRTEM image of a 90° WC/WC GB with a rotation axis of <2$\bar{1}\bar{1}$0>. The {0001} plane of the upper WC grain and the {10$\bar{1}$0} plane of the bottom WC grain are aligned parallel to the GB. Fig. 3B reveals a pronounced segregation of Cr and Co at this GB. The levels of Cr and Co segregation are quantified as the concentration ratio of 4.2 and 3.7, respectively (Fig. 2C and Table S8). Fig. 3C depicts the HRTEM image of another 90° WC/WC GB with a rotation axis of <5$\bar{1}$40>. Here, the {10$\bar{1}$0} plane of the right WC grain aligns with the GB, while the {0001} plane of the left WC grain shows a minor deviation. At this GB, the segregation levels for Cr and Co are notably higher (Fig. 3D), at 6.3 and 7.1 (referenced in Fig. 2C).

Ru segregation is considered moderate compared to Cr and Co segregation at WC/WC GBs, therefore its effect on interfacial strength is less emphasized. To rationalise the observed spatial distribution of Cr and Co and the mechanism behind the exceptional hardness of the 90° $WC_{\{0001\}}$ /$WC_{\{10\bar{1}0\}}$ GB, we performed first-principles simulations based on DFT [30]. To simulate this interface, we constructed a 112-atom $2x\sqrt{3}$ $WC_{\{10\bar{1}0\}}/2 \times 2$ $WC_{\{0001\}}$ model. The in-plane lattice constants of the {10$\bar{1}$0} grain are $a = 0.5836$ nm, $b = 0.5054$ nm, and those of the {0001} grain are $a = 0.5836$ nm, $b = 0.5691$ nm. Consequently, the in-plane lattice mismatch values are 0 % in the *a*-direction, and 11.2 % in the *b*-direction. Under the assumption of pseudomorphic growth, the lattice constants of the interface were taken as $a = 0.5836$ nm, $b = 0.5372$ nm, implying compressive strain in the $WC_{\{10\bar{1}0\}}$ grain and tensile strain in the $WC_{\{0001\}}$ grain. The atomic structure of the relaxed $WC_{\{10\bar{1}0\}}$/$WC_{\{0001\}}$ GB is shown in Fig. 3**E**.

DFT simulations indicate that Cr and Co atoms preferentially substitute W (Table S9) and reside in the $WC_{\{10\bar{1}0\}}$ grain, close to the interface, as depicted in the calculated layer-resolved formation energy map, shown in Fig. 3**F**. This is different to the asymmetric segregation of Co and Ti at the same type of WC/WC GB [31]. Interestingly, Cr atoms prefer to align in the *a*-direction, parallel to the interface. The atomic mismatch between Cr and W leads to further atomic distortion, specifically an additional compressive strain of ~1.5 % in the *a*-direction.

To examine the chemical bonding effects at the interface with and without Cr and Co addition, we calculated the work of separation, shown in Table S10. Our results suggest that Cr and Co addition do not directly enhance the work of separation at this interface. This is expected since W–C bonds are generally stronger than Cr–C or Co–C bonds. Instead, the observed unexpected large hardening effect could be attributed to the fact that, despite the large lattice mismatch in the *b*-direction, the atomic arrangement in the vicinity of the boundary remains well-aligned due to the exceptionally strong W–C covalent bonds (as confirmed by TEM shown in Fig. 3**A**). This alignment induces significant local elastic strain field, manifesting in strong atomic distortion near the interface, as shown by the angle variation shown in Fig. 3**E**. Cr and Co segregation at the boundary further intensifies this effect due to the atomic size mismatch between W and Cr/Co.

Given that the $WC_{\{0001\}}$ and $WC_{\{10\bar{1}0\}}$ planes play a crucial role in the formation of the 90° WC/WC GBs, Figs. 4A and B provide the microstructural details at the $WC_{\{0001\}}$/Co and $WC_{\{10\bar{1}0\}}$/Co phase boundaries, featuring a HAADF–STEM image and corresponding EDXS maps for Co, Cr, and Ru. At both the $WC_{\{0001\}}$/Co and $WC_{\{10\bar{1}0\}}$/Co phase boundaries, $(W,Cr)C_x$ structures are identified. These structures resemble the 'complexion' formations noted in prior studies [32,33], and both show Cr enrichment.

Fig. 4C illustrates the atom distribution maps for the W, C, Co, Ru, and Cr species at a $WC_{\{10\bar{1}0\}}$/Co phase boundary acquired through APT. A sectional analysis of this phase boundary is shown in Fig. 4D, where a 5-nm thick slice was sampled. This section reveals two distinct APT poles: one corresponding to the WC phase with a *d*-spacing of 0.25 nm, and another associated with the Co phase exhibiting a *d*-spacing of 0.20 nm. These observations validate that the extracted region from the WC phase pole, as depicted in Fig. 4D, is indeed the $WC_{\{10\bar{1}0\}}$ plane. Given that the WC/Co interface intersects with the identified plane at ~60°, it is reasonable to believe that the $WC_{\{10\bar{1}0\}}$ plane is also parallel to this WC/Co interface. The 0.20-nm *d*-spacing in the Co phase is consistent with either $Co_{FCC\{111\}}$ or $Co_{HCP\{0002\}}$ plane (Fig. 4E). Fig. 4F presents a

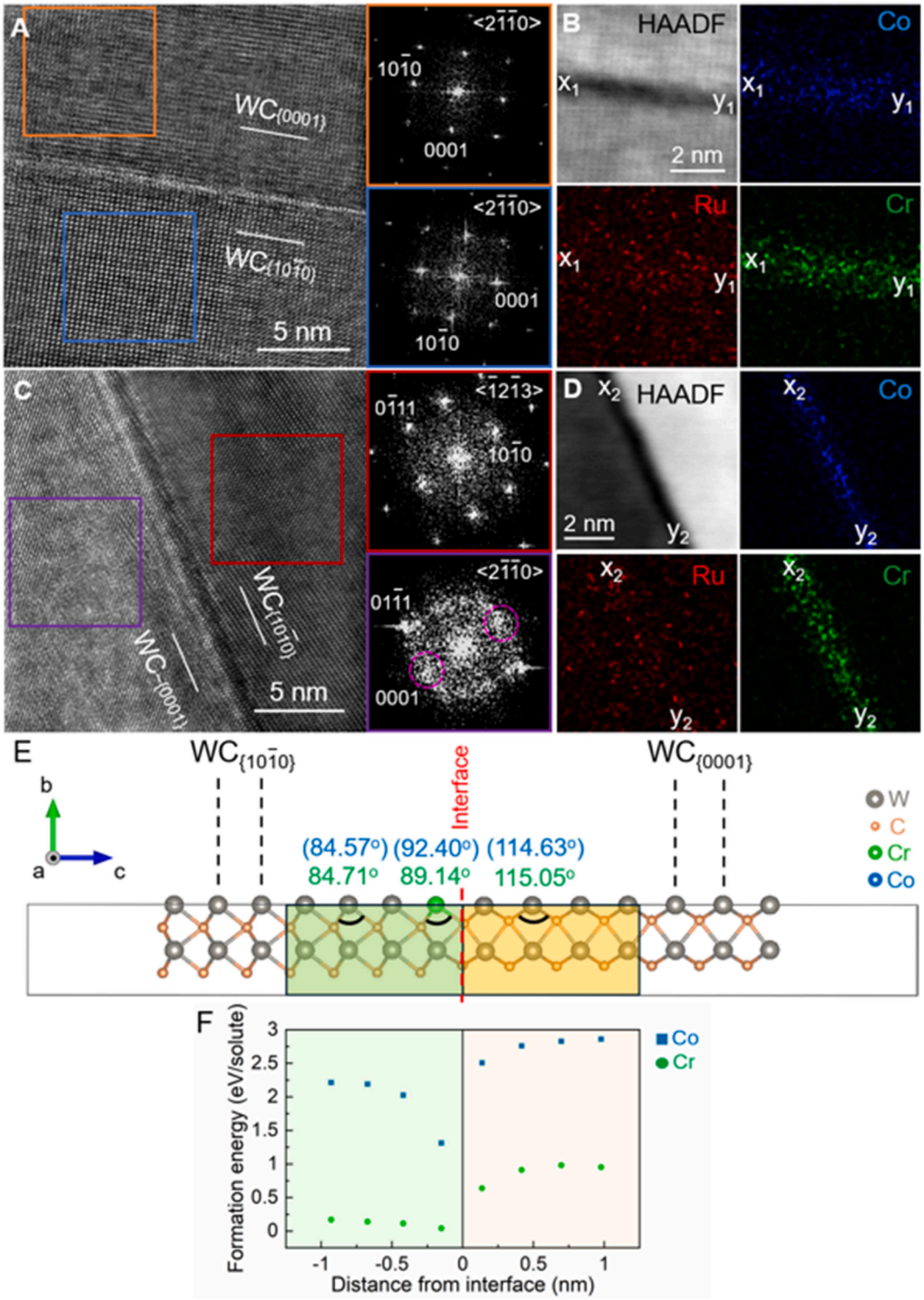


**Fig. 3. High-resolution TEM (HRTEM), STEM–EDXS, and DFT simulation results of the 90° WC/WC GBs, as shown in** Fig. 2. (**A**) HRTEM image of a 90°<2$\bar{1}\bar{1}$0> WC/WC GB. FFT patterns for the neighbouring WC grains are highlighted in orange and blue squares. (**B**) HAADF–STEM image and elemental distribution maps for Co, Ru and Cr at the 90°<2$\bar{1}\bar{1}$0> WC/WC GB. $x_1$ and $y_1$ highlight the position of this GB. (**C**) HRTEM image of a 90°<5$\bar{1}\bar{4}$0> WC/WC GB. FFT patterns for the neighbouring WC grains are highlighted in red and purple squares. (**D**) HAADF–STEM image and elemental distribution maps for Co, Ru and Cr at the 90°<5$\bar{1}\bar{4}$0> WC/WC GB. $x_2$ and $y_2$ highlight the position of this GB. (**E**) DFT simulated the atomic structure of the relaxed $WC_{\{10\bar{1}0\}}/WC_{\{0001\}}$ GB. It comprises one GB plane (dashed red line), $WC_{\{10\bar{1}0\}}$ in green and $WC_{\{0001\}}$ grain in orange, and two corresponding surface slabs. The shaded ranges indicate the range of studied sites for Cr segregation. (F) DFT calculated the layer-resolved formation of energy of Cr and Co substituting W with respect to the interface.

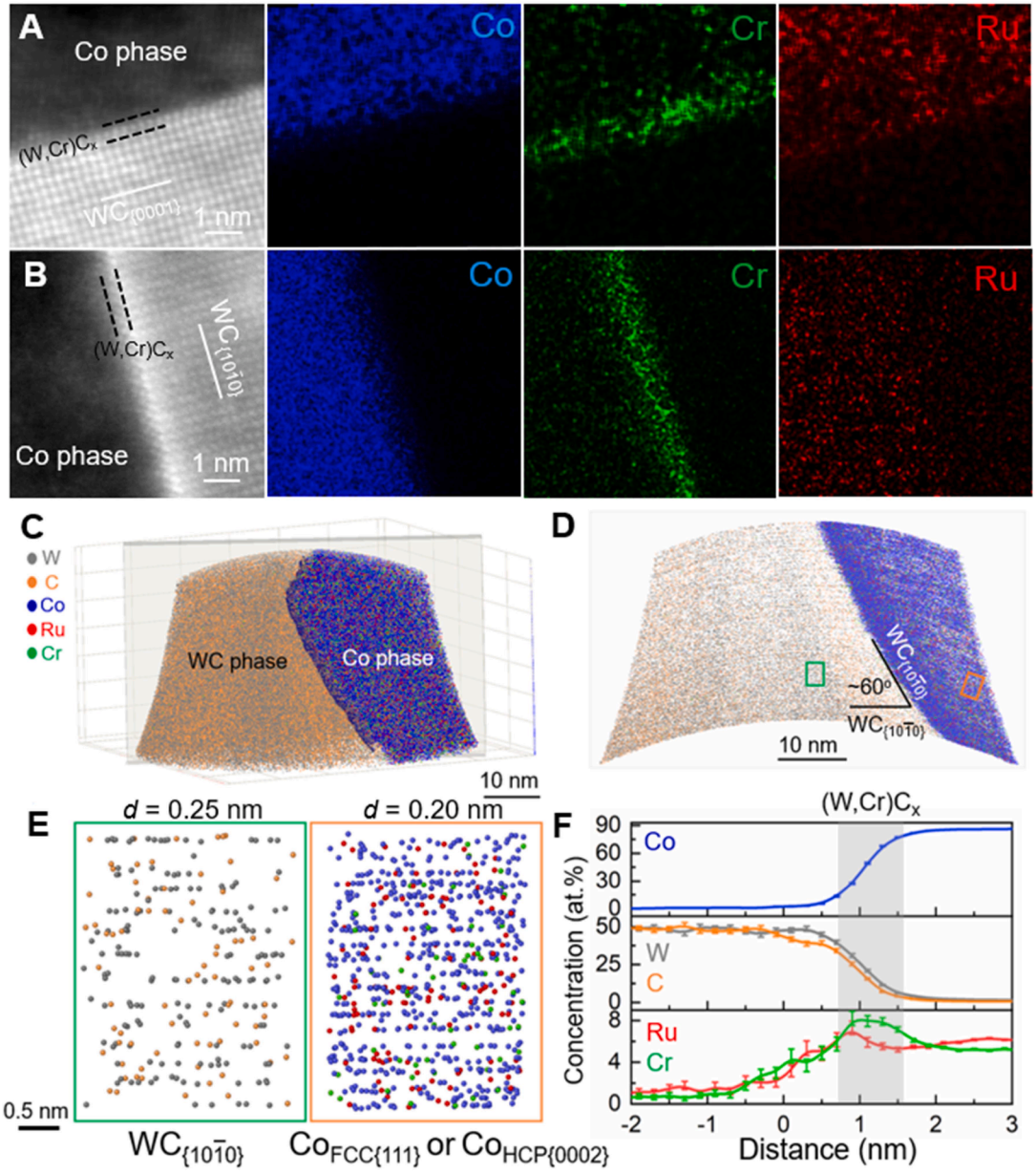


**Fig. 4. STEM–EDXS and APT characterisation of analysis of the $WC_{\{0001\}}$/Co and $WC_{\{10\bar{1}0\}}$/Co phase boundaries in the submicron WC–10Co–1.5Ru–0.6$Cr_3C_2$ cemented carbide.** (**A**) HAADF–STEM image, and corresponding EDXS maps for Co, Cr, and Ru at a $WC_{\{0001\}}$/Co phase boundary. (**B**) HAADF–STEM image, and corresponding EDXS maps for Co, Cr, and Ru at the $WC_{\{10\bar{1}0\}}$/Co phase boundary. (C) Atom distribution maps of W, C, Co, Ru, and Cr at a $WC_{\{10\bar{1}0\}}$/Co phase boundary revealed by APT. A 60 at.% Co isoconcentration surface is used to delineate the $WC_{\{10\bar{1}0\}}$/Co phase boundary. (D) Cross-sectional view of the APT data from (**C**), with green and orange boxes indicating the regions associated with the poles in the WC and Co phase, respectively. (**E**) Enlarged view of the APT dataset within the regions designated by the green and orange boxes, displaying the $WC_{\{10\bar{1}0\}}$ plane and $Co_{FCC\{111\}}$ or $Co_{HCP\{0002\}}$ plane, respectively. (**F**) Proximity histogram derived from the 60 at.% Co isoconcentration surface shown in (**C**).

proximity histogram derived from 60 at.% Co isoconcentration surfaces shown in Fig. 4C. The histogram illustrates a distinct Cr enrichment of ~8 at.% in the $WC_x$ phase at the $WC_{\{10\bar{1}0\}}$/Co phase boundary, corroborating the segregation pattern presented in Fig. 4B.

Fig. 5 illustrates a phenomenological two-WC-particle model for the development of the 90° WC/WC GBs during liquid-phase sintering, delineating three distinct states: heating, soaking, and cooling. Upon heating above the W–Co–C system's liquidus temperature (1300–1360 °C depending on the C level), a Co-rich liquid phase is formed [34]. At the WC/Co liquid interface, Cr atoms preferentially segregate, particularly along the $WC_{\{0001\}}$ and $WC_{\{10\bar{1}0\}}$ planes as depicted in parts A1 and A2 of Fig. 5A [35].

During the soaking state (Fig. 5B), the Co-rich liquid phase wets the WC particles and facilitates mass transport via solution reprecipitation, essential for the WC grain growth. The nucleation of the WC grains predominately occurs at the $WC_{\{0001\}}$ and $WC_{\{10\bar{1}0\}}$ planes, leading to the formation of small islands (B1 and B2 of Fig. 5B). This grain growth progresses through a layer-by-layer growth mechanism, as controlled by solution reprecipitation [36,37]. Consequently, a step-like structure is observed on the $WC_{\{0001\}}$ and $WC_{\{10\bar{1}0\}}$ planes (refer to Fig. S13).

90° WC/WC GBs are formed when the $WC_{\{0001\}}$ and $WC_{\{10\bar{1}0\}}$ planes from two adjacent WC grains come into contact. The Cr atoms, previously attracted along the $WC_{\{0001\}}$ and $WC_{\{10\bar{1}0\}}$ planes, become incorporated at the interface of the newly established 90° WC/WC GB. These WC grains are geometrically characterised as flat triangular prisms with truncated edges. A given complexion is likely stable at high

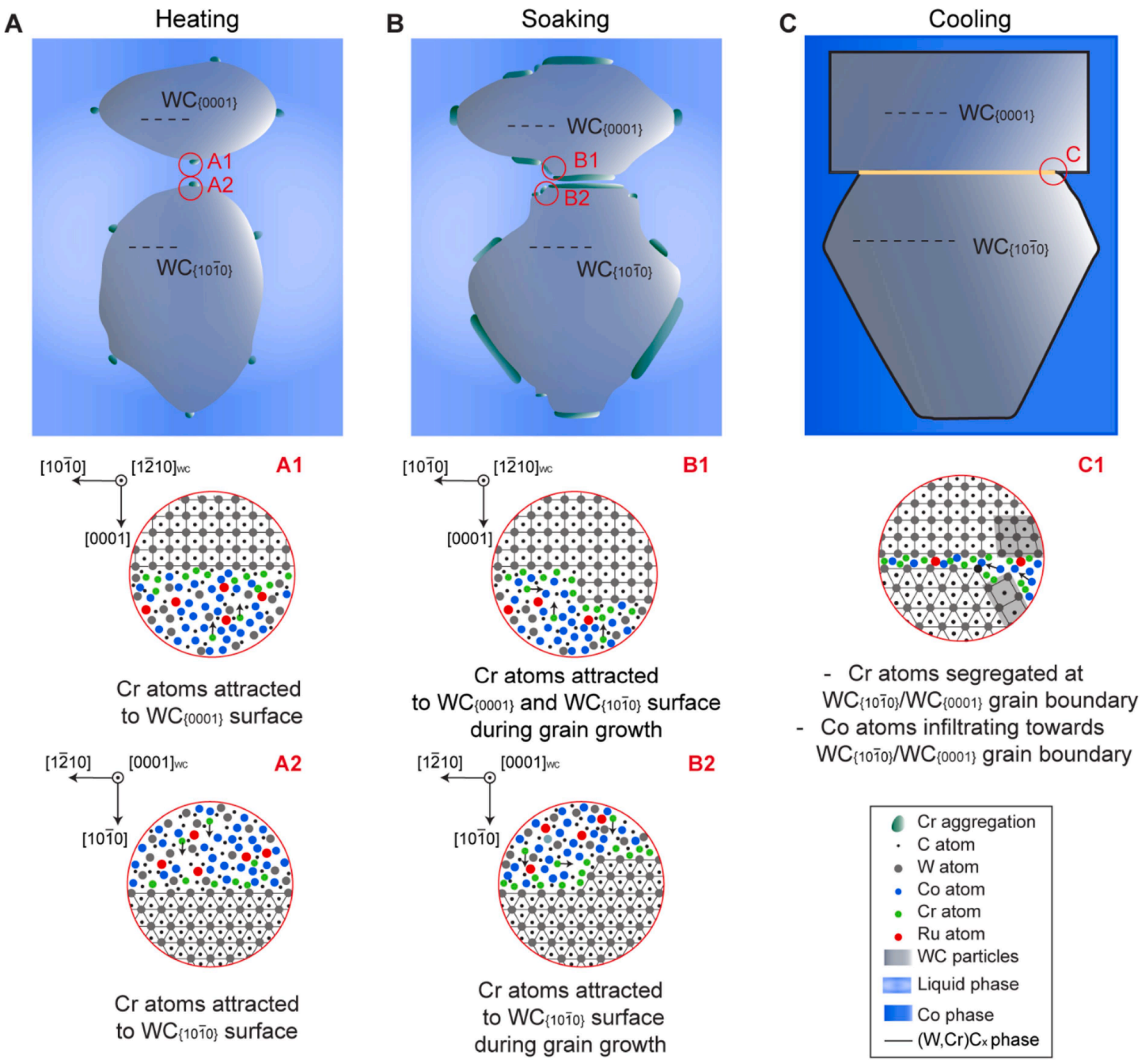


**Fig. 5.** Schematic diagram illustrating the formation of the 90° $WC_{\{0001\}}/WC_{\{10\bar{1}0\}}$ GB with pronounced segregation of Cr and Co. (A) Heating state, (B) Soaking state, and (C) Cooling state.

temperatures. However, if the cooling rate is sufficiently fast, the high-temperature complexion may be kinetically hindered to transform to the lower-temperature state. A pronounced infiltration of Co is the primary contributor to the elevated Co concentration at these 90° WC/WC GBs observed during the cooling phase (Fig. 5C). Subsequently, Cr and Co atoms are substantially incorporated into these 90° WC/WC GBs (C1 of Fig. 5C).

In conclusion, we establish a methodology that harnesses nano-indentation and high-end correlative microscopy techniques to delineate a correlation between local hardness, frequency distribution, and level of elemental segregation at individual GBs in relation to their misorientation angles in a submicron WC–Co cemented carbide. We observe an exceptional hardness attributed to a 90° $WC_{\{0001\}}/WC_{\{10\bar{1}0\}}$ GB. This GB exhibited more pronounced segregations of Cr and Co than other WC/WC GBs. The preferred segregation of Cr and Co is linked to the strong attraction of Cr at the $WC_{\{0001\}}$/Co and $WC_{\{10\bar{1}0\}}$/Co phase boundaries coupled with Co infiltration during liquid-phase sintering. Density functional theory results indicate that a large lattice mismatch, strong W–C covalent bonding, and Cr and Co accumulation generate a robust elastic strain field, resulting in strong atomic distortion near the interface and contributing to exceptional strengthening. These insights provide a foundation for future investigations into grain/phase boundary engineering towards enhancing material hardness.

## CRediT authorship contribution statement

**Hansheng Chen:** Writing – review & editing, Writing – original draft, Visualization, Methodology, Investigation, Formal analysis, Data curation, Conceptualization. **Haoruo Zhou:** Writing – review & editing, Writing – original draft, Visualization, Methodology, Investigation, Formal analysis, Data curation. **Xiangyuan Cui:** Investigation, Methodology, Software, Writing – review & editing. **Christoph Czettl:** Writing – review & editing, Supervision, Investigation, Funding acquisition, Conceptualization. **Thomas Weirather:** Writing – review & editing, Project administration, Investigation. **Julia Pachlhofer:** Writing – review & editing, Investigation. **Pauline Mueller:** Writing – review & editing, Investigation. **Tamara Teppernegg:** Writing – review & editing, Investigation. **Ralph Useldinger:** Writing – review & editing, Investigation. **Sophie Primig:** Writing – review & editing, Investigation, Funding acquisition. **Simon P. Ringer:** Writing – review & editing, Supervision, Resources, Project administration, Investigation, Funding acquisition, Conceptualization.

## Declaration of competing interest

The authors declare that they have no known competing financial interests or personal relationships that could have appeared to influence the work reported in this paper.

## Acknowledgments

The authors acknowledge the facilities, the scientific, and technical assistance provided at Sydney Microscopy & Microanalysis (SMM) and the Sydney Manufacturing Hub (SMH), which are Core Research Facilities at the University of Sydney. We particularly acknowledge Drs. Takanori Sato, Magnus Garbrecht, Vijay Bhatia, Jiangtao Qu, Ranming Niu, Hongwei Liu, Ehsan Farabi, Mrs. Ashalatha Indiradevi, and Ms. Zhifei Zhu. SMM is the university's node of Microscopy Australia. This work was supported by the Australian Research Council (LP190100850). This work was supported by computational resources provided by the Australian Government through the National Computational Infrastructure (NCI, Gadi), and by the Sydney Informatics Hub (the University of Sydney).

## Supplementary materials

Supplementary material associated with this article can be found, in the online version, at doi:10.1016/j.scriptamat.2024.116525.

## References

[1] G. Gottstein, L.S. Shvindlerman, Grain Boundary Migration in Metals: Thermodynamics, Kinetics, Applications, 2nd ed., Taylor & Francis, Boca Raton, 2010.
[2] J. Han, S.L. Thomas, D.J. Srolovitz, Grain-boundary kinetics: a unified approach, Prog. Mater. Sci. 98 (2018) 386–476.
[3] D. Wu, J. Zhang, J.C. Huang, H. Bei, T.G. Nieh, Grain-boundary strengthening in nanocrystalline chromium and the Hall–Petch coefficient of body-centered cubic metals, Scr. Mater. 68 (2) (2013) 118–121.
[4] A. Hussein, A.H.M. Krom, P. Dey, G.K. Sunnardianto, O.A. Moultos, C.L. Walters, The effect of hydrogen content and yield strength on the distribution of hydrogen in steel: a diffusion coupled micromechanical FEM study, Acta Mater. 209 (2021) 116799.
[5] W. Cao, A. Kundu, Z. Yu, M.P. Harmer, R.P. Vinci, Direct correlations between fracture toughness and grain boundary segregation behavior in ytterbium-doped magnesium aluminate spinel, Scr. Mater. 69 (1) (2013) 81–84.
[6] M.A. Arafin, J.A. Szpunar, A new understanding of intergranular stress corrosion cracking resistance of pipeline steel through grain boundary character and crystallographic texture studies, Corros. Sci. 51 (1) (2009) 119–128.
[7] T. Luo, F. Serrano-Sánchez, H. Bishara, S. Zhang, R. Bueno Villoro, J.J. Kuo, C. Felser, C. Scheu, G.J. Snyder, J.P. Best, G. Dehm, Y. Yu, D. Raabe, C. Fu, B. Gault, Dopant-segregation to grain boundaries controls electrical conductivity of n-type NbCoSn half-Heusler alloy mediating thermoelectric performance, Acta Mater. (2021) 217.
[8] X. Ye, F. Yan, L. Schäfer, D. Wang, H. Geßwein, W. Wang, M.R. Chellali, L. T. Stephenson, K. Skokov, O. Gutfleisch, D. Raabe, H. Hahn, B. Gault, R. Kruk, Magnetoelectric tuning of pinning-type permanent magnets through atomic-scale engineering of grain boundaries, Adv. Mater. (Weinheim) 33 (5) (2021) e2006853. -n/a.
[9] N. Petch, The cleavage strength of polycrystals, J. Iron Steel Inst. 174 (1953) 25–28.
[10] E. Hall, The deformation and ageing of mild steel: III discussion of results, Proc. Phys. Soc. Sec. B 64 (9) (1951) 747.
[11] D.M. Saylor, A. Morawiec, G.S. Rohrer, The relative free energies of grain boundaries in magnesia as a function of five macroscopic parameters, Acta Mater. 51 (13) (2003) 3675–3686.
[12] J. García, V. Collado Ciprés, A. Blomqvist, B. Kaplan, Cemented carbide microstructures: a review, Int. J. Refract. Hard Met. 80 (2019) 40–68.
[13] T. Shing, S. Luyckx, I. Northrop, I. Wolff, The effect of ruthenium additions on the hardness, toughness and grain size of WC–Co, Int. J. Refract. Hard Met. 19 (1) (2001) 41–44.
[14] H. Zeng, W. Liu, C. Wei, Influence of Ru on the microstructure and performance of WC-Co cemented carbides, Mater. Sci. Technol. 38 (13) (2022) 940–946.
[15] S. Luyckx, M.Z. Alli, Comparison between $V_8C_7$ and $Cr_3C_2$ as grain refiners for WC-Co, Mater. Des. 22 (6) (2001) 507–510.
[16] H. Tian, M. Zhang, Y. Peng, Y. Du, P. Zhou, Sintering behavior and mechanical properties of $Cr_3C_2$ doped ultra-fine WC-Co cemented carbides: experment guided with thermodynamic calculations, Int. J. Refract. Hard Met. 78 (2019) 240–246.
[17] H. Tian, Y. Peng, Y. Du, Y. Zhang, S. Zhang, J. Zheng, Optimization of the mechanical properties of ultra-fine WC-Co-$Cr_3C_2$ cemented carbides via an approach based on thermodynamic calculations and characterization of the experimental results by the Weibull distribution, Calphad 70 (2020) 101778.
[18] A. Henjered, M. Hellsing, H.-O. Andrén, H. Nordén, Quantitative microanalysis of carbide/carbide interfaces in WC–Co-base cemented carbides, Mater. Sci. Technol. 2 (8) (1986) 847–855.
[19] J. Vicens, M. Benjdir, G. Nouet, A. Dubon, J. Laval, Cobalt intergranular segregation in WC-Co composites, J. Mater. Sci. 29 (1994) 987–994.
[20] M. Christensen, G. Wahnström, Strength and reinforcement of interfaces in cemented carbides, Int. J. Refract. Hard Met. 24 (1–2) (2006) 80–88.
[21] M. Christensen, G. Wahnström, Effects of cobalt intergranular segregation on interface energetics in WC–Co, Acta Mater. 52 (8) (2004) 2199–2207.
[22] X. Zhou, A. Ahmadian, B. Gault, C. Ophus, C.H. Liebscher, G. Dehm, D. Raabe, Atomic motifs govern the decoration of grain boundaries by interstitial solutes, Nature Commun 14 (1) (2023) 3535.
[23] M. Herbig, D. Raabe, Y. Li, P. Choi, S. Zaefferer, S. Goto, Atomic-scale quantification of grain boundary segregation in nanocrystalline material, Phy. Rev. Lett. 112 (12) (2014) 126103.
[24] S.R. Kalidindi, S.J. Vachhani, Mechanical characterization of grain boundaries using nanoindentation, Curr. Opin. Solid State Mater. Sci. 18 (4) (2014) 196–204.
[25] P.E. Blöchl, Projector augmented-wave method, Phys. Rev. B 50 (24) (1994) 17953.
[26] J.P. Perdew, K. Burke, M. Ernzerhof, Generalized gradient approximation made simple, Phys. Rev. Lett. 77 (18) (1996) 3865.
[27] G. Kresse, J. Furthmüller, Efficient iterative schemes for ab initio total-energy calculations using a plane-wave basis set, Phys. Rev. B 54 (16) (1996) 11169.
[28] S. Lay, Evaluation of slip transfer through WC grain boundaries in cemented carbides, Int. J. Refract. Hard Met. 99 (2021) 105584.
[29] M. Elizalde, I. Ocaña, J. Alkorta, J. Sánchez-Moreno, Mechanical strength assessment of single WC-WC interfaces present in WC-Co hardmetals through micro-beam bending experiments, Int. J. Refract. Hard Met. 72 (2018) 39–44.
[30] X.-Y. Cui, S.P. Ringer, On the nexus between atom probe microscopy and density functional theory simulations, Mater. Charact. 146 (2018) 347–358.
[31] Z. Luo, C. Hu, L. Xie, H. Nie, C. Xiang, X. Gu, J. He, W. Zhang, Z. Yu, J. Luo, A highly asymmetric interfacial superstructure in WC: expanding the classic grain boundary segregation and new complexion theories, Mater. Horiz. 7 (1) (2020) 173–180.
[32] X. Liu, X. Song, H. Wang, X. Liu, F. Tang, H. Lu, Complexions in WC-Co cemented carbides, Acta Mater 149 (2018) 164–178.
[33] C. Yang, C. Hu, C. Xiang, H. Nie, X. Gu, L. Xie, J. He, W. Zhang, Z. Yu, J. Luo, Interfacial superstructures and chemical bonding transitions at metal-ceramic interfaces, Sci. Adv. 7 (11) (2021) eabf6667.
[34] H. Exner, Physical and chemical nature of cemented carbides, Int. Met. Rev. 24 (1) (1979) 149–173.
[35] M. Yousfi, S. Norgren, H.-O. Andrén, L. Falk, Chromium segregation at phase boundaries in Cr-doped WC-Co cemented carbides, Mater. Charact. 144 (2018) 48–56.
[36] Y. Zhong, L.L. Shaw, Growth mechanisms of WC in WC–5.75 wt% Co, Ceram. Int. 37 (8) (2011) 3591–3597.
[37] E. Fransson, M. Gren, G. Wahnström, Complexions and grain growth retardation: first-principles modeling of phase boundaries in WC-Co cemented carbides at elevated temperatures, Acta Mater. 216 (2021) 117128.